Scientific Reports

https://doi.org/10.1038/s41598-026-39360-3

Article in Press

Optical, luminescence and magnetic properties of braunite–rhodonite nanocomposites synthesized by green aqueous sol–gel route

Received: 25 December 2025

Accepted: 4 February 2026

Published online: 13 March 2026

Cite this article as: Nagy M.G.Y., Ibrahim F.A. & Abo-Naf S.M. Optical, luminescence and magnetic properties of braunite–rhodonite nanocomposites synthesized by green aqueous sol–gel route. *Sci Rep* (2026). https://doi.org/10.1038/s41598-026-39360-3

Mai G. Y. Nagy, F. A. Ibrahim & S. M. Abo-Naf

We are providing an unedited version of this manuscript to give early access to its findings. Before final publication, the manuscript will undergo further editing. Please note there may be errors present which affect the content, and all legal disclaimers apply.

If this paper is publishing under a Transparent Peer Review model then Peer Review reports will publish with the final article.

ARTICLE IN PRESS

© The Author(s) 2026. **Open Access** This article is licensed under a Creative Commons Attribution 4.0 International License, which permits use, sharing, adaptation, distribution and reproduction in any medium or format, as long as you give appropriate credit to the original author(s) and the source, provide a link to the Creative Commons licence, and indicate if changes were made. The images or other third party material in this article are included in the article's Creative Commons licence, unless indicated otherwise in a credit line to the material. If material is not included in the article's Creative Commons licence and your intended use is not permitted by statutory regulation or exceeds the permitted use, you will need to obtain permission directly from the copyright holder. To view a copy of this licence, visit http://creativecommons.org/licenses/by/4.0/.

ARTICLE IN PRESS

Optical, luminescence and magnetic properties of braunite–rhodonite nanocomposites synthesized by green aqueous sol–gel route

Mai G. Y. Nagy [1], F. A. Ibrahim [1,*], S. M. Abo-Naf [2]

[1] Department of Physics, Faculty of Science, Arish University, Al-Arish, 45511, Egypt

[2] Glass Research Department, National Research Centre (NRC), El-Buhouth St., Dokki, 12622 Cairo, Egypt

* Corresponding author; F. A. Ibrahim

E-mail address: fahmed_ibrahim@yahoo.com

ARTICLE IN PRESS

Abstract

Braunite (Mn_7SiO_{12}) –rhodonite ($MnSiO_3$) nanocomposites have been synthesized utilizing a green aqueous citrate sol–gel route. The influence of heat-treatment temperature on the structure and properties of these nanocomposites was investigated. X-ray diffraction and high resolution transmission electron microscopy analyses demonstrated that well-crystallized nanoparticles, having average sizes in the range of 18–42 nm, were produced. $MnSiO_3$-content increased in the nanocomposites with increasing calcination temperature from 600 to 900 °C. Optical, photoluminescence and magnetic properties were determined. Ultraviolet-visible-near infrared diffuse reflectance

ARTICLE IN PRESS

spectra were used, applying Kubelka-Munk function, for optical absorbance calculation and determination of the band gap energy (E_g). Optical absorption spectra exhibited bands at 415–438 nm originated from Mn^{2+} ions, and other bands at 550 and 599 nm due to absorption of Mn^{3+} ions. E_g was found to increase with increasing $MnSiO_3$-content in the nanocomposites. The obtained nanocomposites gave green fluorescence emissions at 525–565 nm, a yellow emission at 584 nm and red emissions at 619 nm. All the synthesized nanocomposites exhibited antiferromagnetic properties in which the paramagnetic contribution and magnetization increased as the $MnSiO_3$-content increased. The present nanocomposites are promising candidates for application as light emitting diodes as well as magnetoelectronic materials which are used in biomedical applications.

ARTICLE IN PRESS

Keywords: Manganese–silicates; Sol–gel; XRD-HRTEM; Photoluminescence; Antiferromagnetism; Optical materials

---

1. Introduction

Compared to their microscopic and macroscopic counterparts, nanomaterials possess distinctive features giving rise to a wide range of

ARTICLE IN PRESS

intriguing properties and superior applications[1,2]. This is due to their high surface-to-volume ratio and quantum confinement effects. The size-dependent optical band gap of semiconductor nanomaterials demonstrates how quantum confinement significantly alters their optical, electrical and magnetic characteristics. These remarkable characteristics have drawn a lot of continuous research interest in various technological fields such as biomedicine, energy conversion, catalysis and sensing[1–3]. Although single-component nanomaterials provide beneficial features, more control and flexibility in modifying their properties and functionalities offer rather more superiority for a variety of cutting-edge technologies. Using multiphases nanocomposites is an effective strategy for such purpose[4]. The synergy between various phases can produce functionalities not found in the single-phase material.

Silicates are versatile materials with a wide range of applications, largely due to their ability to be produced in various stoichiometric forms. The silanol groups on the surface of silica, in particular, improve its functionality and make it ideal for biomedical uses like bone regeneration, orthopedic coatings and drug delivery systems[5–8]. Manganese (Mn), a trace element that is vital to human health, has recently drawn great interest for use in biomedical applications due to its unique magnetic and luminescent properties. Mn-containing magnetic nanostructures have demonstrated large potential in magnetic hyperthermia treatment and magnetic resonance imaging (MRI) contrast agent. Nanoparticles are used in this treatment to produce heat and kill tumor cells only, causing the

ARTICLE IN PRESS

least amount of harm to healthy tissue. The low toxicity and abundance of Mn make it even more appealing for these applications[5,9–13]. Moreover, mesoporous manganese silicate ($MnSiO_3$ in majority)-coated silica nanoparticles can be used as a controlled drug delivery system for the chemotherapy drug doxorubicin and as a multi-stimuli-responsive MRI contrast agent. Both in vitro and in vivo, these nanoparticles demonstrated exceptional efficacy as a T_1-MRI contrast agent and offered on-demand drug release[14]. At atmospheric pressure, the binary phases in manganese-silicate ($MnO–SiO_2$) system are tephroite (Mn_2SiO_4) which is also known as manganese orthosilicate, rhodonite ($MnSiO_3$) and braunite (Mn_7SiO_{12})[15]. Mn_2SiO_4 is an olivine-type compound. Olivines have chemical compositions corresponding to the formula M_2SiO_4, where M can denote one chemical element or a combination of different ones, and have an orthorhombic crystal structure[16]. Typically only at high pressures and temperatures, $MnSiO_3$ has a perovskite structure of chemical formula ABO_3 with eightfold A cation, sixfold B cation and oxygen, respectively[17,18]. At ambient conditions, i.e. room temperature and pressure, $MnSiO_3$ has a pyroxenoid silicate structure. Mn_7SiO_{12} has been the center of controversies concerning its chemical formula, its crystal phase and space group, the role of oxidation and the silica state of manganese. Eventually, its formula was found to be $Mn^{2+}Mn_6^{3+}SiO_{12}$, i.e. it contains di- and tri-valent Mn. It can also be expressed by the structural formula $MnSiO_3.3Mn_2O_3$[15,19]. Therefore, Mn_7SiO_{12} can be considered as manganese silicate composite comprising three molecules

ARTICLE IN PRESS

of Mn_2O_3 oxide. Braunite has a distorted perovskite-like structure. According to previous research[5,17], the synthesis of a single-phase $MnSiO_3$ at ambient conditions represents a significant challenge as the process can result in the formation of multiple phases. In order to form a pure phase of $MnSiO_3$, oxygen high pressure was necessary and the synthesis process had to be carried out at high temperatures between 1673 and 2073 K. It might be expected that, even for MnO: SiO_2 system with stoichiometric ratio of 1:1, formation of braunite-rhodonite composite seems to be inevitable. Therefore, the main objective of the current work is to investigate the product of this system at atmospheric pressure.

The choice of synthesis route has a significant influence on phase formation and, consequently, on the properties exhibited by produced silicates. Several synthesis methods such as conventional solid-state reactions, hydrothermal, coprecipitation, sol–gel and many others were described in the past literature. A distinctive and adaptable bottom-up chemical synthesis for creating a wide range of nanostructures, especially metal oxides, is the sol–gel methodology. Through a sequence of irreversible chemical reactions, this low-temperature processing turns molecular precursors into solid materials. Creating a stable colloidal solution, i.e. sol, and then turning it into a continuous three-dimensional network, i.e. gel, constitutes the two primary steps in its fundamental principle. Because of its affordability and capacity to produce high-purity materials with high degree of homogeneity, well-controlled shapes and

ARTICLE IN PRESS

nano-scale particle size distributions, this approach is frequently favored in both academia and industrial applications[20–22].

Based on the above considerations, the aim of present work was to investigate the structure and properties of the product of MnO–SiO_2 system with stoichiometric ratio of 1:1 at atmospheric pressure using a facile and green aqueous citrate sol–gel synthetic route. The optical, band gap energy, photoluminescence and magnetic properties have been measured. The effect of increasing temperature of heat-treatment, from 600 to 900 °C, on the structure and formed phases as well as the investigated properties was studied. This temperature range is very abundant in sol–gel industries where great benefits from the above mentioned advantages of this methodology can be attained for manufacture of advanced new materials possessing superior properties.

ARTICLE IN PRESS

2. Materials and methods

2.1. Materials

Analytical reagent grade chemicals were used in the present sol–gel synthesis. These chemicals are tetraethyl orthosilicate (TEOS, $C_8H_{20}O_4Si$, or Si $(OC_2H_5)_4$), 99.6% purity, was purchased from Merck, Germany. Anhydrous manganese (II) acetate (Mn $(Ac)_2$, $C_4H_6O_4Mn$, or Mn $(CH_3COO)_2$), +98% purity, was bought from Acros organics. Absolute ethanol (EtOH, C_2H_5OH), +99% extra pure, was purchased from Fisher Scientific, UK. Hydrochloric acid (HCl), 37% certified AR for analysis, was bought from Roth Chemie GmbH,

ARTICLE IN PRESS

Germany. Anhydrous citric acid (CA, $C_6H_8O_7$, or $CH_2COOH{-}C(OH)COOH{-}CH_2COOH$), in the form of white powder of 99% purity, was purchased from Win lab, UK. Double distilled water (H_2O) was used all-over the synthesis process.

2.2. Sol–gel synthesis process

In the current procedure, aqueous citrate green chemical route was employed, which benefited from the solubility of anhydrous Mn $(Ac)_2$ in water. In the sol–gel reactions, TEOS and anhydrous Mn $(Ac)_2$ was used as precursors for SiO_2 and MnO, respectively. Hence, appropriate weights of these precursors, equivalent to MnO:SiO_2 system with stoichiometric ratio of 1:1, were adopted. In order to avoid fast hydrolysis reaction of Mn and immediate precipitation of its hydroxide, Mn $(OH)_2$, aqueous Mn $(Ac)_2$ solution was firstly chelated by aqueous citric acid (CA) solution. In typical preparation, Mn $(Ac)_2$ was first dissolved in H_2O with a weight (Wt.) ratio of 1:4 of Mn $(Ac)_2$ and H_2O, respectively. Another solution of CA readily dissolved in H_2O with a Wt. ratio of 1:2.5 of CA and H_2O, respectively, was prepared. These two solutions were mixed together under continuous magnetic stirring at room temperature (RT) for 30 min. Separately, TEOS was partially hydrolyzed by mixing it with EtOH and H_2O, under continuous stirring at RT for only 10 min (not more), in an acid catalyst of 1M HCl until reaching acidic condition of pH= 3. The solution pH was detected and controlled by means of a pH-meter and step-wise addition of

ARTICLE IN PRESS

the HCl solution. The molar ratio of TEOS: EtOH: H2O was 1:8:0.5, respectively. This solution was added to the Mn $(Ac)_2$–CA aqueous solution and kept under stirring at RT for 30 min where a clear sol was obtained. It is noteworthy to mention that the resultant sol was prepared in a relatively excess H_2O diluted condition in order to well-control the sol–gel reactions rate. Gelation was initiated via warming this sol at 60–65 °C. After 30 min, a white gel was formed which was then dried at 95 °C for 20 h. At this temperature, EtOH and H_2O were evaporated where their evaporation temperatures are 78 and 95–100 °C, respectively. For removal of CA, drying was further continued at 200 °C for 10 h. CA has no definite evaporation temperature, i.e. no boiling point. Instead, it decomposes at 175–185 °C into H_2O and CO_2, rather than evaporation as an intact compound. Thereafter, the dried gel was subjected to heat-treatment at three different temperatures which are 600, 750 and 900 °C for 4 h, according to the proposed study, and the products were then characterized. Raise of temperature from 200 °C to the respective one was performed employing a slow heating rate of 1 °C/min. Table 1 lists the chemical composition, sample code and heat-treatment temperature (T) of synthesized materials. It is worth to mention that reproducibility of the present preparation route is very good and the characterization results have consistency percentage of about 95–98% for three times preparation.

ARTICLE IN PRESS

ARTICLE IN PRESS

2.3. Characterization techniques

The formed crystalline phases in synthesized materials were identified utilizing powder X-ray diffraction (XRD) analysis using a Bruker D8 Discover diffractometer equipped with a Ni-filtered Cu-K_α X-ray radiation source (λ= 1.5406 Å) powered at 45 kV and 30 mA. Diffractograms were recorded in the 2θ range from 10º to 70º. The DIFFRAC.SUITE software was employed for instrument control and data analysis. The reference intensity ratio (RIR) calculations were utilized in order to correlate quantitatively the percentage of constituting phases in each composition.

High resolution transmission electron microscope (HRTEM) was used to study the morphology and size of the synthesized nanocomposites employing a JEOL JEM-2100 (Japan) microscope operated at accelerating voltage of 200 kV with a resolution of 1.402 Å. The very fine powder of each sample was dispersed in pure ethanol and sonicated for 10 min. Then, the well-dispersed suspension was dropped on a carbon-coated copper microgrid and inserted into the TEM chamber for depiction. Lattice interlayer *d*-spacing was investigated by recording the inverse fast Fourier transformation (IFFT) profiles.

Optical properties of the prepared nanocomposites were studied by measuring the ultraviolet-visible-near infrared (UV–Vis–NIR) diffuse reflectance spectra (DRS), in the wavelength range of 200-2500 nm, applying the Kubelka-Munk function for optical absorbance calculation and

ARTICLE IN PRESS

determination of the band gap energy (E_g) using a spectrophotometer type T80 PG Instruments, England.

Room temperature photoluminescence (PL) emission and excitation spectra of the synthesized Mn_7SiO_{12}–$MnSiO_3$ nanocomposites were recorded using a fluorescence spectrophotometer (Jasco FP-6500, Japan) equipped with a xenon flash lamp as the excitation light source.

Room temperature magnetization (M) and magnetic hysteresis (M-H) loops of the studied nanocomposites were measured using vibrating sample magnetometer (VSM; LakeShore 7410, USA) under applied magnetic field between –20 and 20 kOe.

ARTICLE IN PRESS

3. Results and discussion

3.1. Structural XRD investigation

Fig. 1 shows XRD patterns of the produced materials after calcination at 600, 750 and 900 °C. Crystalline phases constituting the synthesized materials, their ratio and their average crystallite size (D) calculated from XRD results are listed in Table 2. D was calculated using Scherrer's equation[21,23] as following:

$$D = 0.9 \lambda / (\beta \cos\theta)$$

where λ is X-ray wavelength of the employed Cu-K_α source (λ= 1.5406 Å), θ is the Bragg angle of the corresponding peak, β is the full width at half maxima (FWHM). The given D is the average value calculated from the three strongest diffraction peaks.

ARTICLE IN PRESS

The diffractograms of all the produced materials, i.e. MS600, MS750 and MS900, demonstrated the formation of braunite (Mn_7SiO_{12})–rhodonite ($MnSiO_3$) composites with varying ratios. As mentioned in Table 2, it was found from the analytical XRD calculations that increasing of the calcination temperature from 600 to 900 °C resulted in increase of the $MnSiO_3$ fraction in the formed composites from 34.6 to 45.2%, while that of Mn_7SiO_{12} decreased from 65.4 to 54.8%. As indicated in Fig. 1, this can be also observed in the relative increase of most intense diffraction peak of $MnSiO_3$ which is accompanied by a relative decrease of that peak of Mn_7SiO_{12}. The formed braunite phase was found to agree with that one of reference code COD 9006541 with the tetragonal $I4_1/acd$ space group and space group No. 142 whose standard lattice constants are a=b= 9.4264 Å and c= 18.6962 Å. The main diffraction peaks of this phase were recorded at 2θ= 32.98°, 55.32°, 65.70°, 38.16°, 55.07° and 66.16° which correspond to Bragg reflection planes of (-2-2-4), (-40-8), (-6-2-4), (-400), (-4-40) and (-2-2-12), respectively. These crystal planes correspond, in turn, to *d*-spacing values of 2.714, 1.659, 1.420, 2.357, 1.666 and 1.411 Å. The rhodonite phase was found to match that one of reference code COD 9003676 with the triclinic C-1 space group and space group No. 2 whose standard lattice constants are a= 9.8381 Å, b= 10.5361 Å and c= 12.2381 Å. The main diffraction peaks of this phase were recorded at 2θ= 32.34°, 30.46°, 30.01°, 28.41°, 41.38° and 33.74° which correspond to Bragg reflection planes of (-2-24), (-1-1-3), (-310), (-13-1), (-24-1) and (0-2-3),

ARTICLE IN PRESS

respectively. These reflection planes correspond to *d*-spacing values of 2.766, 2.932, 2.975, 3.139, 2.180 and 2.655 Å. It is important to mention that no impurity phases were detected in the present XRD patterns and, hence, interpretation of the property trends was merely correlated with the detected Mn_7SiO_{12} and $MnSiO_3$ phases. As expected, the average crystallite size (D) increased with increasing of the calcination temperature and it was found to be in the range of 20–42 nm, as listed in Table 2. The deviation from chemical stoichiometry of $MnSiO_3$ formation occurred because Mn^{2+} can be readily oxidized to Mn^{3+} in air and aqueous solutions resulting in formation of $(Mn_2O_3)_3MnSiO_3=Mn_7SiO_{12}$[24]. This is why, Mn_7SiO_{12} was termed braunite structure of rhodonite in some published articles[25,26].

3.2. HRTEM analysis

For further demonstration of morphology of the as-synthesized Mn_7SiO_{12}–$MnSiO_3$ nanocomposites, HRTEM analysis was utilized. The nanostructure of MS600 is depicted in Fig. 2. Its TEM image, shown in Fig. 2a, indicates that its average particle size is about 18 nm. Fig. 2b depicts its fine lattice fringes indicating interplanar *d*-spacing of 0.27 nm which corresponds to the (-2-2-4) crystallographic plane of Mn_7SiO_{12}. This lattice image was further confirmed by its IFFT profile, given in Fig. 3, which also indicates *d*-spacing of 0.2691 nm. Fig. 4a shows the TEM image of MS750 nanocomposite. This figure indicates that its average particle size is about 30 nm. Fig. 4b presents its high

ARTICLE IN PRESS

resolution lattice image that shows *d*-spacing of 0.28 nm which corresponds to the (-2-24) reflection plane of $MnSiO_3$ at $2\theta = 32.34°$. This lattice image was also confirmed by its IFFT profile, shown in Fig. 5, which indicates *d*-spacing of 0.279 nm[27,28]. TEM image of MS900 nanocomposite is shown in Fig. 6a which indicates average particle size of about 42 nm. Fig. 6b depicts its high resolution lattice image that shows *d*-spacing of 0.27 nm which corresponds to the (-2-24) reflection plane of $MnSiO_3$. The latter was ascertained by the corresponding IFFT profile that also shows *d*-spacing of 0.275 nm as given in Fig. 7[27,28]. The selected area electron diffraction (SAED) patterns of the MS600, MS750 and MS900 nanocomposites, shown in Fig. 8a,b,c. respectively, reveal high degree of crystallinity and confirm the polycrystalline nature of these nanocomposites. Collectively, it can be pointed out that both XRD results and TEM observations are in a very good consistency and support each other.

ARTICLE IN PRESS

3.3. UV–Vis–NIR DRS and band gap energy

From the measured UV-Vis-NIR DRS, optical absorbance was calculated and the absorbance spectra of the MS600, MS750 and MS900 nanocomposites are shown in Fig. 9. These spectra are very broad and, hence, were deconvoluted into their constituting Gaussian peaks. The resultant peaks located in three ranges which are 262–286, 415–438 and 550–599 nm whose interpretation was made in view of many past literature[29–36]. The bands at 262 and 286 nm in the UV region can be attributed to either the silicate intrinsic absorption or the

ARTICLE IN PRESS

$^6A_1(S) \rightarrow {}^4E(^4D)$ and $^6A_1(S) \rightarrow {}^4T_2(^4D)$ charge transfer transitions of Mn^{2+} ions from its ground state $^6A_1(S)$ to its conduction band. Overlapped absorptions of both of these latter two absorptions can take place simultaneously. The bands at 415, 431 and 438 nm in the visible region can be assigned to the $^6A_{1g} \rightarrow [^4A_{1g}, {}^4E_g]$ electronic transitions of Mn^{2+} ions. The peaks at 550 and 599 nm in the visible region can be ascribed to the $^5E_g \rightarrow {}^5T_{2g}$ electronic transition of the octahedrally coordinated Mn^{3+} ions in braunite (Mn_7SiO_{12}). Notable shifts occurred in the absorption features as the synthesis temperature increased from 600 to 900 °C. Mn^{2+} related peaks were shifted from 438 nm (in sample MS600) to 421 nm (MS750) then to 415 nm (MS900), which indicates changes in the Mn^{2+} local environment caused by thermal treatment. This blue shift indicates a shift in the intensity of crystal field or site symmetry surrounding the Mn^{2+} ions, which could be brought about by enhanced crystallinity or changes in bond lengths and angles as the temperature was raised. Furthermore, at the highest synthesis temperatures (i.e. 900 °C), the peak at 415 nm for MS900 exhibited the highest intensity indicating a larger concentration or more uniform incorporation of Mn^{2+} ions in the lattice due to the increase of rhodonite ($MnSiO_3$) content.

For determination of the optical band gap, Kubelka-Munk equation was used to translate the diffuse reflectance, R, into a parameter proportional to the absorption coefficient (α) as follows:

$$\alpha / S = (1 - R)^2 / 2R = F(R)$$

ARTICLE IN PRESS

where S is the scattering, which is nearly constant with respect to the radiation wavelength. As a result, the ratio α /S, or simply F(R), gives information about how α behaves in relation to the wavelength of radiation. Thus, Tauc's plots were built to determine the band gap values of the powders, assuming that $\alpha \approx F(R)$, as follows[37–39]:

$$F(R)h\nu = \alpha h\nu = A\,(h\nu - E_g)^{n}$$

$$i.e. \quad (F(R)h\nu)^{1/n} = (\alpha h\nu)^{1/n} = A\,(h\nu - E_g)$$

where h is the Planck's constant, ν is the frequency of photons, A is the proportionality constant, E_g is the optical band gap in (eV) of the semiconductor and n= 1/2 for direct allowed transition which was experimentally determined. Therefore, Fig. 10 gives the Tauc's plots, of $(\alpha h\nu)^2$ as a function of photon energy $(h\nu)$, of the studied MS600, MS750 and MS900 nanocomposites from which E_g was determined via extrapolation of the linear portion of plot to zero ordinate. The obtained E_g values are 0.935, 0.994 and 1.242 eV for MS600, MS750 and MS900, respectively, and are also given in Table 1. Thus, this consistent rise in band gap with increasing synthesis temperature, and in turn increasing $MnSiO_3$ content, suggests increased crystallinity and structural evolution. This resulted in fewer defect states and more electronic separation between the valence and conduction bands. The increased energy gap indicates a tendency toward more semiconducting behavior, which means that carrier mobility and conductivity properties change with temperature affording promising potential for optoelectronic and photocatalytic applications[40,41].

ARTICLE IN PRESS

3.4. PL emission and excitation spectra

PL is considered one of the most powerful analytical tools especially in the field of optical, electronic and optoelectronic applications. In PL, a material absorbs photons typically in the UV or visible region resulting in excitation of electrons from the ground state to higher electronic excited states. These electrons then lose some energy and relaxed to a lower excited state through non-radiative processes, e.g. vibrational relaxation, before returning to the ground state producing emission of photons at certain wavelengths corresponding to the energy difference between the states. Therefore, this emission process typically includes excitation, relaxation and radiative emission[42–49]. Fig. 11 shows the room temperature fluorescence emission spectra, excited at 254 nm of the manganese silicate MS600, MS750 and MS900 nanocomposites. MS600 sample exhibited two broad peaks which are a green emission band centered at 562 nm and a red emission at 619 nm. MS750 nanocomposite exhibited two broad green emissions at 525 and 565 nm, with a very weak shoulder at 619 nm. The spectrum of MS900 reveals two broad bands which are a green emission at 533 nm showing considerably higher intensity, and a yellow emission at 584 nm with relatively weaker intensity. For the manganese ions, although they exist in di- and tri-valent states, i.e. Mn^{2+} and Mn^{3+}, within the studied Mn_7SiO_{12}–$MnSiO_3$ nanocomposites, the observed fluorescence states are attributed only to Mn^{2+} active centers, exhibiting green and red emissions in the tetrahedral and octahedral coordination's,

ARTICLE IN PRESS

respectively[35]. The electronic configuration of Mn^{2+} is $3d^5$ which has high spin of S= 5/2. Its emission bands arise from transitions between the spin-orbit components of the $^4T_1$ excited state and the $^6A_1$ ground state. Position of these emission bands is considerably dependent on the structural surroundings of Mn^{2+} ions within the lattice[30]. Therefore, all the obtained green, yellow and red emission bands are assigned to the $^4T_1(^4G) \rightarrow ^6A_1(^6S)$ d–d intra-transition of Mn^{2+} ions[30,35,50–52]. The radiative recombination is described by excitation of electrons located in the ground state $^6A_1(^6S)$ to the conduction band of Mn_7SiO_{12}–$MnSiO_3$ nanocomposite lattice. Then, these electrons relax by a non-radiative process from the $^4T_1(^4G)$ excited level. Finally, a charge transfer to ground state $^6A_1(^6S)$ results in the obtained emissions[52]. This fluorescence emission mechanism is schematically illustrated by the energy levels diagram shown in Fig. 12. From the present fluorescence spectra, it can be concluded that increasing of the calcination temperature, i.e. increased $MnSiO_3$ concentration in the nanocomposite, favors the formation of tetrahedrally coordinated Mn^{2+} ions. This is evident by conversion of the red band at 619 nm in sample MS600 into a very weak shoulder in MS750 and then its disappearance in MS900 as well as by the highest intensity of green band at 533 nm. The obtained PL tunable visible emissions may be beneficial for light emitting diodes (LED) technology, optoelectronic devices, bio-imaging probes and photonic applications.

Fig. 13 shows the PL excitation spectra of MS600, MS750 and MS900 nanocomposites monitored at λ_{em}= 560, 560 and 533 nm, respectively. In all the

ARTICLE IN PRESS

spectra, two sharp and intense peaks were recorded at 254 and 470 nm. The first peak has noticeably higher intensity. It can be seen that peak intensity increased monotonically with increasing of the temperature from 600 to 900 °C. The intense UV excitation peak at 254 nm is assigned to the $^6A_1(S) \rightarrow {}^4E({}^4D)$ and $^6A_1(S) \rightarrow {}^4T_2({}^4D)$ transitions of Mn^{2+} ions which represents the primary absorption edge and is typical of manganese ions interaction with the silicate lattice. The moderate visible excitation peak at 470 nm is caused by the $^6A_{1g} \rightarrow [{}^4A_{1g}, {}^4E_g]$ electronic transitions of Mn^{2+} ions[31,33,35,36,41,50]. The recorded excitation peaks indicate effective energy absorption routes that might allow for flexible optical behavior appropriate for use in luminous devices and sensors.

ARTICLE IN PRESS

3.5. Magnetic properties

Fig. 14 shows the room temperature magnetic M–H hysteresis loops of MS600, MS750 and MS900 nanocomposites. The inset graph indicates their narrow hysteresis loops with non-vanishing coercivity and remanence. The corresponding magnetization parameters; saturation magnetization (Ms), coercivity (Hc) and remanent magnetization (Mr); are given in Table 3. From this figure, it is indicated that these manganese silicate nanocomposites exhibited antiferromagnetic (AFM) behavior with considerable paramagnetic (PM) contribution. The latter increased with the increase of temperature, and thereby the increase of $MnSiO_3$ concentration. Accordingly, Ms increased from 0.7199 to 0.8365 to 0.9809 emu/g and, conversely, Hc decreased from 47.01 to

ARTICLE IN PRESS

19.04 to 14.61 Oe in cases of MS600, MS750 and MS900, respectively. In Mn-based AFM materials, the magnetic spins of adjacent Mn^{2+} ions align in opposite, or antiparallel, directions leading to a nearly zero net magnetization below a specific Néel temperature (T_N). This behavior is often mediated by superexchange through non-magnetic atoms such as oxygen[53]. In previous publications[54,55], it was considered that the magnetism of Mn-based compounds can be strongly influenced by the Mn–Mn distance and AFM ordering was attributed to the close proximity of Mn atoms that caused direct exchange coupling between Mn atoms owing to their nearly half-filled *3d* orbitals. It was pointed out that Mn atoms result in AFM when the distance of Mn–Mn atoms is less than 2.9 Å. Another interpretation for AFM of the metallic compound $L1_0$-MnAl τ-phase was correlated with excess Mn atoms in the composition which occupy Al sites. This Mn occupancy ratio of the Al site leads to AFM coupling with Mn atoms in the Mn sites, i.e. superexchange interaction between the magnetic atoms through hybridization with the *p*-orbital electrons of a non-magnetic ligand or atom[55]. This situation can be also considered and viewed in the current Mn_7SiO_{12}–$MnSiO_3$ nanocomposites between the Mn^{2+} ions and Si atoms. Furthermore, the present AFM with PM contribution might be explained in terms of mixed magnetic phases embodying the coexistence of magnetically ordered and non-ordered Mn sites[56,57]. In AFM nanomaterials, long-range AFM ordering is often disturbed at the particle surface. Therefore, AFM of the Mn_7SiO_{12}–$MnSiO_3$ nanocomposites can be attributed to the uncompensated

ARTICLE IN PRESS

magnetic moment existed at the grain boundary which varies with different grain size distributions. This difference is, consequently, responsible for the change of Ms values. In such cases, variation of the coercivity depends on the surface and anisotropy[58]. Very recently, AFM spintronics have garnered significant attention due to the utilization of AFM as an efficient and controllable spin source[59]. Because of the exchange springs in AFM/PM bilayers, AFM moments can be controlled by a very small magnetic field. Therefore, the charge-spin conversion mediated by AFMs affords remarkable advances in the tunable spin generation, transport, manipulation and detection based on the control and probe of AFM moments. AFMs have several advantages such as negligible stray field, robustness to the disturbing magnetic field, and intrinsic high frequency (terahertz (THz) range) of spin dynamics. Therefore, AFMs have promising potential for application as ultrahigh-density magnetic memories with a fast writing speed and low energy consumption, nanoscale oscillators within the THz range, and AFM-based neuromorphic computing[59]. Moreover, based on their high sensitivity, much finer control over activation and assembly, and biocompatibility, AFMs can be used in many biological applications such as the magnetomechanical destruction of cancer cells, drug delivery and cell separation. Their self-assembly behavior in fluid environments is very beneficial in areas such as microfluidics and biosensing[60,61]. Nano-sized magnetic materials are expected to exhibit better efficiency, than their bulk counterparts, due to the unique combination of

ARTICLE IN PRESS

beneficial reduction in grain size, increased surface area, size-dependent properties and quantum confinement effects. It is possible to control not only the nano-size but also the morphology of the nanoparticles by proper choice of material composition and synthesis methodology. Therefore, superior properties can be tailored via the large number of very active atoms or/and ions present at the surface which result in tunable surface chemistry of the nano-structured materials. Moreover, incorporation of magnetic nanoparticles within matrices, such as polymers, ceramics or other materials, yields advanced nanocomposites with enhanced magneto-responsive properties[62–66].

As mentioned in the experimental section, the present sol–gel processing route possesses a very good reproducibility. Normally, when such nanocomposites products are applied in industry, continuous characterization analyses are performed for each produced batch before marketing. Moreover, the current Mn_7SiO_{12}–$MnSiO_3$ nanocomposites are reliable for transition metals or/and rare earth ions doping and codoping for tailoring of tunable optical and magnetic properties. Future work complementing these ideas is in progress by our research team.

ARTICLE IN PRESS

Limitations

This study is limited by [e.g., the restricted range of synthesis temperatures/compositions, the absence of in situ structural characterization during the sol–gel process, and the use of bulk-averaged magnetic measurements]. These factors may influence the generalizability of the observed

ARTICLE IN PRESS

optical, luminescence and magnetic behaviors to other processing conditions or compositions. Future work including [e.g., in situ measurements, extended composition ranges, or advanced microscopic and spectroscopic techniques] will be valuable to further elucidate the structure–property relationships in braunite–rhodonite nanocomposites.

Conclusions

In summary, a very facile green aqueous citrate sol–gel route was exploited for synthesis of Mn_7SiO_{12}–$MnSiO_3$ nanocomposites at different calcination temperatures whose influences on the phase structure, optical, photoluminescence and magnetic properties of these nanocomposites were studied. XRD and HRTEM analyses demonstrated that well-crystallized nanoparticles, having average sizes in the range of 18–42 nm, were produced. It was found that $MnSiO_3$-content increased in the nanocomposites with increasing calcination temperature from 600 to 900 °C. Optical absorption spectra exhibited bands at 415–438 nm originated from Mn^{2+} ions, and other bands at 550 and 599 nm due to absorption of Mn^{3+} ions. E_g was found to increase with increasing $MnSiO_3$-content in the nanocomposites. Tunable green fluorescence emissions at 525–565 nm, a yellow emission at 584 nm and red emissions at 619 nm were obtained. The obtained PL visible emissions and AFM properties may be beneficial for light emitting diodes (LED) technology, optoelectronic devices, bio-imaging probes, photonic applications and AFM spintronics.

ARTICLE IN PRESS

ARTICLE IN PRESS

Declaration of Competing Interest

The authors declare that they have no known competing financial interests or personal relationships that could have appeared to influence the work reported in this paper.

Funding:

No funding was received for this work.

Data availability:

All data supporting the findings of this study are available within the article.

The datasets generated and/or analyzed during the current study are available from the corresponding author on reasonable request.

ARTICLE IN PRESS

References

1. Li, J. & Zhang, J. Z. Optical properties and applications of hybrid semiconductor nanomaterials. *Coordin. Chem. Rev.* **253**, 3015–3041 (2009).
2. Asha, A. B. & Narain, R. Nanomaterials properties. in *Elsevier eBooks* (eds. et al.) 343–359 (Elsevier, 2020).
3. Lowry, G. V., Gregory, K. B., Apte, S. C. & Lead, J. R. Transformations of nanomaterials in the environment. *Environ. Sci. Technol.* **46**, 6893–6899 (2012).
4. Omanović-Mikličanin, E., Badnjević, A., Kazlagić, A. & Hajlovac, M. Nanocomposites: a brief review. *Health Technol.* **10**, 51–59 (2019).

ARTICLE IN PRESS

5. De Sá, M. R. et al. Magnetic and fluorescent manganese silicate nanostructures for advanced applications. *ChemistrySelect* **10**, e02098 (2025).

6. Zhang, S., Zhang, T., Dong, B., Chen, J. & Meng, C. Synthesis and characterization of manganese silicate nanostructures. *Colloids Surf. A* **630**, 11–20 (2023).

7. Turcer, L. & Padture, N. P. High-performance ceramic composites. *Scr. Mater.* **154**, 111–117 (2018).

8. Galgo, S. J. C. et al. Increase of soil organic carbon stock by iron slag-based silicate fertilizer application in paddy soils. *Agric. Ecosyst. Environ.* **365**, 108924 (2024).

9. Salian, A. et al. Advanced ceramic technologies and applications. *Int. J. Appl. Ceram. Technol.* **20**, 2635–2660 (2023).

10. Wang, Q., Zhang, Y., Jiang, H., Li, X., Cheng, Y. & Meng, C. Electrochemical properties of manganese silicate composites. *Chem. Eng. J.* **362**, 818–829 (2019).

11. Li, Y. et al. High-performance electrode materials for energy storage. *Chem. Eng. J.* **455**, 140773 (2023).

12. Spoialà, A. et al. Magnetite-silica core/shell nanostructures: from surface functionalization towards biomedical applications–a review. *Appl. Sci.* **11**, 11075 (2021).

13. Arango-Ospina, M., Nawaz, Q. & Boccaccini, A. R. Bioactive materials for regenerative medicine. *Regen. Med.* **25**, 255–273 (2020).

14. Li, X., Zhao, W., Liu, X., Chen, K., Zhu, S., Shi, P., Chen, Y. & Shi, J. Mesoporous manganese silicate coated silica nanoparticles as multi-

ARTICLE IN PRESS

stimuli-responsive T_1-MRI contrast agents and drug delivery carriers. *Acta Biomater.* **30**, 378–387 (2015).

15. Huang, J.-H. & Rosén, E. Determination of Gibbs free energies of formation for the silicates $MnSiO_3$, Mn_2SiO_4 and Mn_7SiO_{12} in the temperature range 1000–1350 K by solid state emf measurements. *Phys. Chem. Miner.* **21**, 228–233 (1994).

16. Tang, Q. & Dieckmann, R. Floating-zone growth and characterization of single crystals of manganese orthosilicate, Mn_2SiO_4. *J. Cryst. Growth* **361**, 89–97 (2012).

17. Fujino, K., Suzuki, K., Hamane, D., Seto, Y., Nagai, T. & Sata, N. High-pressure phase relation of $MnSiO_3$ up to 85 GPa: existence of $MnSiO_3$ perovskite. *Am. Mineral.* **93**, 653–657 (2008).

18. Fujino, K., Nishio-Hamane, D., Suzuki, K., Izumi, H., Seto, Y. & Nagai, T. Stability of the perovskite structure and possibility of the transition to the post-perovskite structure in $CaSiO_3$, $FeSiO_3$, $MnSiO_3$ and $CoSiO_3$. *Phys. Earth Planet. Int.* **177**, 147–151 (2009).

19. Haghjoo, H., Sangsefidi, F. S., Hashemizadeh, S. A. & Salavati-Niasari, M. Investigation of the magnetic properties and the photocatalytic activity of synthesized Mn_7SiO_{12} nanostructures by green capping agent. *J. Mol. Liq.* **225**, 290–295 (2017).

20. Kolahalam, L. A., Viswanath, I. K., Diwakar, B. S., Govindh, B., Reddy, V. & Murthy, Y. Review on nanomaterials: synthesis and applications. *Mater. Today Proc.* **18**, 2182–2190 (2019).

21. Alorabi, G. A. M., Abdelwahab, S. M. & Abo-Naf, S. M. Sol–gel synthesis, structure, ferromagnetism and optical properties of Mn–doped

ARTICLE IN PRESS

titania diluted magnetic semiconductors nanoparticles. *Egyptian J. Chem.* **65**, 431–446 (2022).

22. Bokov, D. et al. Nanomaterial by sol–gel method: synthesis and application. *Adv. Mater. Sci. Eng.* **2021**, 5102014 (2021).

23. Majumder, T., Das, D. & Majumder, S. B. Investigations on the electrochemical characteristics of electrophoretically deposited $NiTiO_3$ negative electrode for lithium-ion rechargeable cells. *J. Phys. Chem. Solids* **158**, 110239 (2021).

24. Cheng, Y., Zhang, Y., Wang, Q. & Meng, C. Synthesis of amorphous $MnSiO_3$/graphene oxide with excellent electrochemical performance as supercapacitor electrode. *Colloids Surf. A* **562**, 93–100 (2019).

25. Wang, L., Shi, M., Yang, C., Liu, Y., Jiang, J., Dai, K., Guo, Z. & Yan, C. Amorphous $MnSiO_3$ confined in graphene sheets for superior lithium-ion batteries. *J. Alloy. Compd.* **804**, 243–251 (2019).

26. Li, B. et al. Mixed-valent $MnSiO_3$/C nanocomposite for high-performance asymmetric supercapacitor. *J. Colloid Interface Sci.* **556**, 239–248 (2019).

27. Dong, X., Zhang, Y., Chen, Q., Jiang, H., Wang, Q., Meng, C., Kou, Z. Ammonia-etching-assisted nanotailoring of manganese silicate boosts faradaic capacity for high-performance hybrid supercapacitors. *Sustain. Energy Fuels* **4**, 2220–2228 (2020).

28. Jiang, H., Zhang, Y., Wang, C., Wang, Q., Meng, C. & Wang, J. Rice husk-derived Mn_3O_4/manganese silicate/C nanostructured composites for high-performance hybrid supercapacitors. *Inorg. Chem. Front.* **6**, 2788–2800 (2019).

ARTICLE IN PRESS

29. Marzouk, M. A. & Abo-Naf, S. M. Structure characterization and photoluminescence of sol-gel synthesized Ag-Dy-codoped silica phosphor. *J. Non-Cryst. Solids* **505**, 292–300 (2019).

30. Abo-Naf, S. M., Marzouk, M. A., Abdel-Hameed, S. A. M., Fayad, A. M. & Hamdy, Y. M. Variable photoluminescence and magnetic behaviors of Mn-Ho-codoped silicate glasses synthesized by sol-gel processing. *J. Lumin.* **216**, 116743 (2019).

31. Morad, I., Liu, X. & Qiu, J. Surface crystallized Mn-doped glass-ceramics for tunable luminescence. *J. Am. Ceram. Soc.* **102**, 5843–5852 (2019).

32. Mbule, P. S., Ntwaeaborwa, O. M., Mothudi, B. M. & Dhlamini, M. S. Structural and optical characterization of nanoparticulate manganese doped zinc silicate phosphors prepared by sol–gel and combustion methods. *J. Lumin.* **179**, 74–82 (2016).

33. Omri, K., El Ghoul, J., Alyamani, A., Barthou, C. & El Mir, L. Luminescence properties of green emission of SiO_2/Zn_2SiO_4:Mn nanocomposite prepared by sol–gel method. *Physica E* **53**, 48–54 (2013).

34. Li, P., Peng, M., Wondraczek, L., Zhao, Y., Viana, B. Red to near infrared ultralong lasting luminescence from Mn^{2+}-doped sodium gallium aluminum germanate glasses and (Al, Ga)-albite glass-ceramics. *J. Mater. Chem. C* **3**, 3406–3415 (2015).

35. Abul-Magd, A. A., Basry, A. A. H., Abu El Hassan, S. M. & Abu-Khadra, A. S. Interplay between structural modifications and optical/luminescence response in Mn-doped alkali borate glasses. *Mater. Chem. Phys.* **288**, 126381 (2022).

36. Abo-Naf, S. M. & Marzouk, M. A. Tunable blue and green emissions of sol–gel synthesized transparent nano-willemite codoped with nano-

ARTICLE IN PRESS

pyroxmangite and dysprosium. *Nano-Struct. Nano-Objects* **26**, 100685 (2021).

37. Moghiminia, S., Farsi, H. & Raissi, H. Comparative optical and electrochemical studies of nanostructured $NiTiO_3$ and $NiTiO_3$–TiO_2 prepared by a low temperature modified sol–gel route. *Electrochim. Acta* **132**, 512–523 (2014).

38. Dias, J. A., Freire, A. L. F., Girotto, I., Roveri, C. D., Mastelaro, V. R., Paris, E. C. & Giraldi, T. R. Phase evolution and optical properties of nanometric Mn-doped TiO_2 pigments. *Mater. Today Commun.* **27**, 102295 (2021).

39. Azab, A. A., Esmail, S. A. & Abdelamksoud, M. K. Studying the effect of cobalt doping on optical and magnetic properties of zinc oxide nanoparticles. *Silicon* **11**, 165–174 (2018).

40. Sronsri, C., Sittipol, W. & U-Yen, K. Luminescence characterization of Mn-doped $LiMgPO_4$ synthesized using different precursors. *J. Solid State Chem.* **297**, 122083 (2021).

41. Rao, M. J., Murthy, K. S. R., Kumar, C. R. S., Singh, B. P., Choudary, G. S. V. R. K. & Varma, M. C. Photoluminescence properties of manganese activated calcium tungstate phosphors. *Dig. J. Nanomater. Biostruct.* **19**, 761–771 (2024).

42. Mohamed, M., Jayiz, M., Alshammari, A. S., Sedky, A. & Khan, Z. R. Comparative study on structural, morphological, optical and photocatalytic properties of Mn_3O_4/ZnO, CuO/ZnO and Fe_2O_3/ZnO nanocomposites. *Opt. Quantum Electron.* **55**, 562 (2023).

ARTICLE IN PRESS

43. Li, J., Tian, X., Bao, W., Zhao, J. & Jiang, Z. Recent advances in the development and applications of lanthanide-based luminescent materials: a comprehensive review. *Discover Appl. Sci.* **7**, 1310 (2025).

44. Sedky, A., Afify, N., Ali, A. M. & Algarni, H. FTIR, optical and photoluminescence investigation of $Zn_{1-x}RE_xO$ nanoparticles for optical and power operation devices. *J. Electroceramics* **49**, 33–52 (2022).

45. Mehtab, A., Ahmed, J., Alshehri, S. M., Mao, Y. & Ahmad, T. Rare earth doped metal oxide nanoparticles for photocatalysis: a perspective. Nanotechnology **33**, 142001 (2022).

46. Fazil, M., Ahmed, J. & Ahmad, T. Enhanced photo/electrocatalytic efficiency of Zn-decorated TiO_2 nanostructures for sustainable hydrogen evolution. *Catal. Today* **445**, 115103 (2025).

47. Abbady, G., Afify, N., Sedky, A. & Hamad, D. Effect of annealing temperature on structural, optical and magnetic properties of $Cd_{1-x}Mn_xZnO_2$ nanocomposites: An investigation for ferromagnetic. *Ceram. Int.* **49**, 18042–18054 (2023).

48. Mohamed, M., Jaradat, E. K., Alshammari, A. S. & Sedky, A. Enhanced optical, dielectric and ferromagnetic properties in ZnO/M nanocomposites for advanced device applications. *Sci. Rep.* **15**, 40353 (2025).

49. Jain, S. K., Pandit, N. A., Fazil, M., Ali, S. A., Ahmed, J., Alshehri, S. M., Mao, Y. & Ahmad, T. Chemical fabrication, structural characterization and photocatalytic water splitting application of Sr-doped SnO_2 nanoparticles. *Nanotechnology* **33**, 355706 (2022).

50. Gao, D., Kuang, Q., Gao, F., Xin, H., Yun, S. & Wang, Y. Achieving opto-responsive multimode luminescence in $Zn_{1+x}Ga_{2-2x}Ge_xO_4$: Mn

ARTICLE IN PRESS

persistent phosphors for advanced anti-counterfeiting and information encryption. *Mater. Today Phys.* **27**, 100765 (2022).

51. Xu, Y., Huang, W., Deng, C. & Hou, Q. Dual-mode multicolor luminescence anti-counterfeiting based on Mn-doped color-tunable $MgGa_2O_4:Zn^{2+}/Ge^{4+}$ phosphors. *J. Solid State Chem.* **317**, 123695 (2023).

52. Bessadok, M. N., Ananias, D., Bouri, A., Bouzidi, C., Barthou, C. & El Mir, L. Effect of doping element on non-contact luminescence thermometry properties of nanocomposite SiO_2/Zn_2SiO_4:X (X = Mn, V, Ca). *J. Lumin.* **269**, 120480 (2024).

53. Lv, B., Si, M., Cheng, L., Yan, Z., Li, X. & Gao, C. New noncollinear antiferromagnet Mn_3Al for antiferromagnetic spintronics. *Acta Mater.* **290**, 120939 (2025).

54. Sakuma, A. & Fukamichi, K. Antiferromagnetism of Mn alloys. in *Handbook of Advanced Magnetic Materials* (eds. Liu, Y. *et al.*) 914–975 (Springer, Berlin, 2005).

55. Sato, S., Irie, S., Nagamine, Y., Miyazaki, T. & Umeda, Y. Antiferromagnetism in perfectly ordered $L1_0$-MnAl with stoichiometric composition and its mechanism. *Sci. Rep.* **10**, 12489 (2020).

56. Lacroix, C. Quantum magnetism in low dimensions. *J. Phys. Soc. Jpn.* **79**, 011008 (2010).

57. Gottschilch, M., Gourdon, O., Persson, J., de la Cruz, C., Petricek, V. & Brueckel, T. Magnetic ordering and crystal structure of complex intermetallics. *J. Mater. Chem.* **22**, 15275–15285 (2012).

ARTICLE IN PRESS

58. Tursun, R., Su, Y., Yu, Q. & Tan, J. Room-temperature coexistence of electric and magnetic orders in $NiTiO_3$ and effect of ethylene glycol. *Mater. Sci. Eng. B* **228**, 96–102 (2018).

59. Bai, H., Zhang, Y. C., Han, L., Zhou, Y. J., Pan, F. & Song, C. Antiferromagnetism: an efficient and controllable spin source. *Appl. Phys. Rev.* **9**, 041316 (2022).

60. Welbourne, E. N., Vemulkar, T. & Cowburn, R. P. High-yield fabrication of perpendicularly magnetised synthetic antiferromagnetic nanodiscs. *Nano Res.* **14**, 3873–3878 (2021).

61. Wani, I. A., Ahmad, T. & Khosla, A. Recent advances in anticancer and antimicrobial activity of silver nanoparticles synthesized using phytochemicals and organic polymers. *Nanotechnology* **32**, 462001 (2021).

62. Ahmad, T., Ramanujachary, K. V., Lofland, S. E. & Ganguli, A. K. Nanorods of manganese oxalate: a single source precursor to different manganese oxide nanoparticles (MnO, Mn_2O_3, Mn_3O_4). *J. Mater. Chem.* **14**, 3406–3410 (2004).

63. Ahmad, T., Lone, I. H. & Ubaidullah, M. Structural characterization and multiferroic properties of hexagonal nano-sized $YMnO_3$ developed by a low temperature precursor route. *RSC Adv.* **5**, 58065–58071 (2015).

64. Chand, K. & Vasquez-Guardado, E. S. Magnetic Nanoparticles: Synthesis and Applications in Life Sciences. *ChemistryOpen* **14**, e202500214 (2025).

65. Sedky, A., Afify, N., Abbas, A. & Abd-Elrahim, G. Cooperative effects due to Zn–Sn replacement by Co-ions on the optical and magnetic

ARTICLE IN PRESS

properties of $(ZnSn)_{1-x}Co_xO$ nanocomposites. *Mater. Chem. Phys.* **313**, 128776 (2024).

66. Sedky, A. et al. Annealing temperature effect on structural, mechanical, and magnetic properties of $Cd_{0.40}M_{0.60}ZnO_2$ (M = Mn, Ni) nanocomposites. *Mater. Chem. Phys.* **309**, 128326 (2023).

Figures

ARTICLE IN PRESS

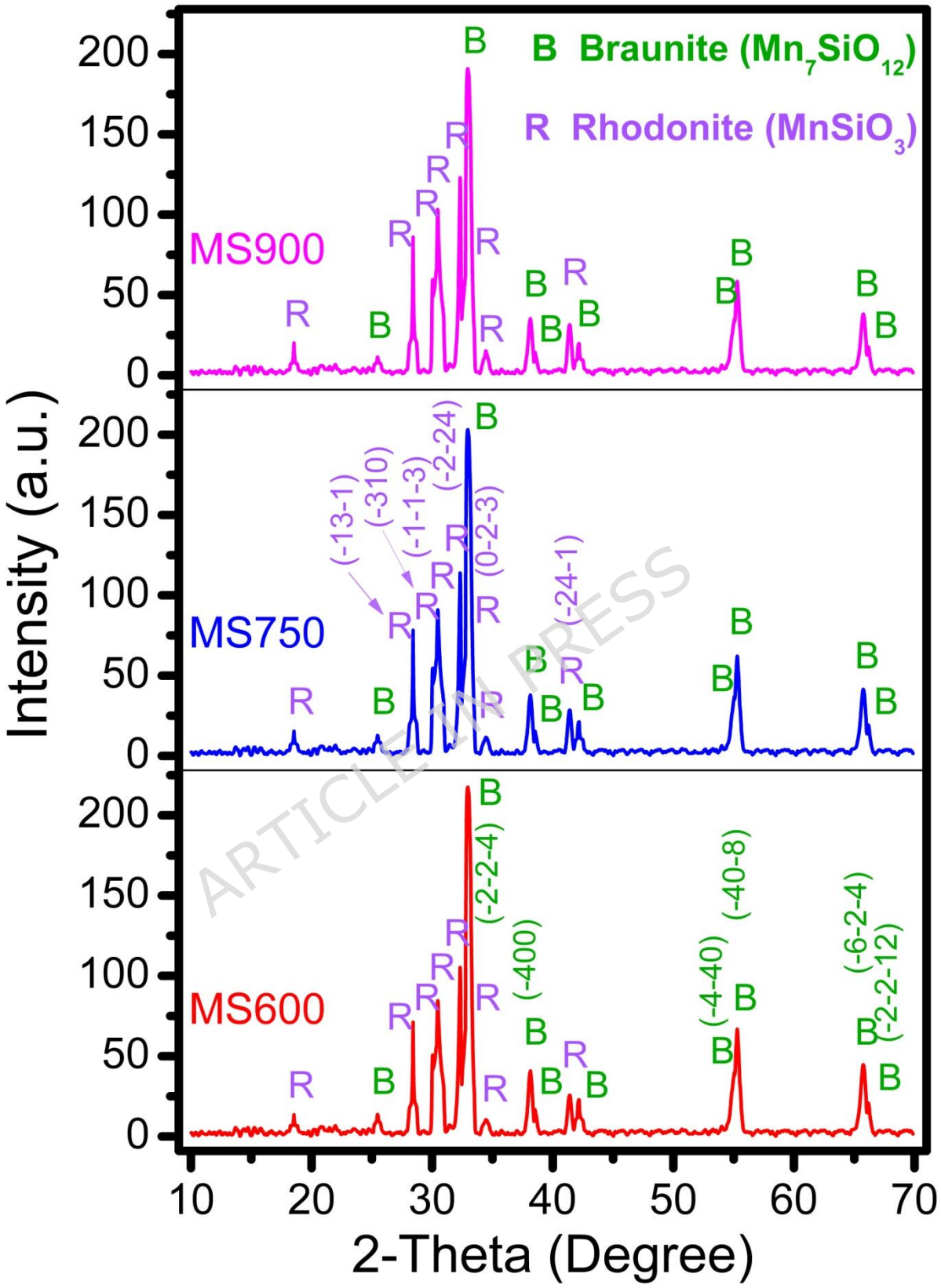

B Braunite (Mn_7SiO_{12})
R Rhodonite ($MnSiO_3$)
MS900
MS750
MS600
Intensity (a.u.)
2-Theta (Degree)
(-13-1)
(-310)
(-1-1-3)
(-2-24)
(0-2-3)
(-24-1)
(-2-2-4)
(-400)
(-4-40)
(-40-8)
(-6-2-4)
(-2-2-12)

Fig. 1

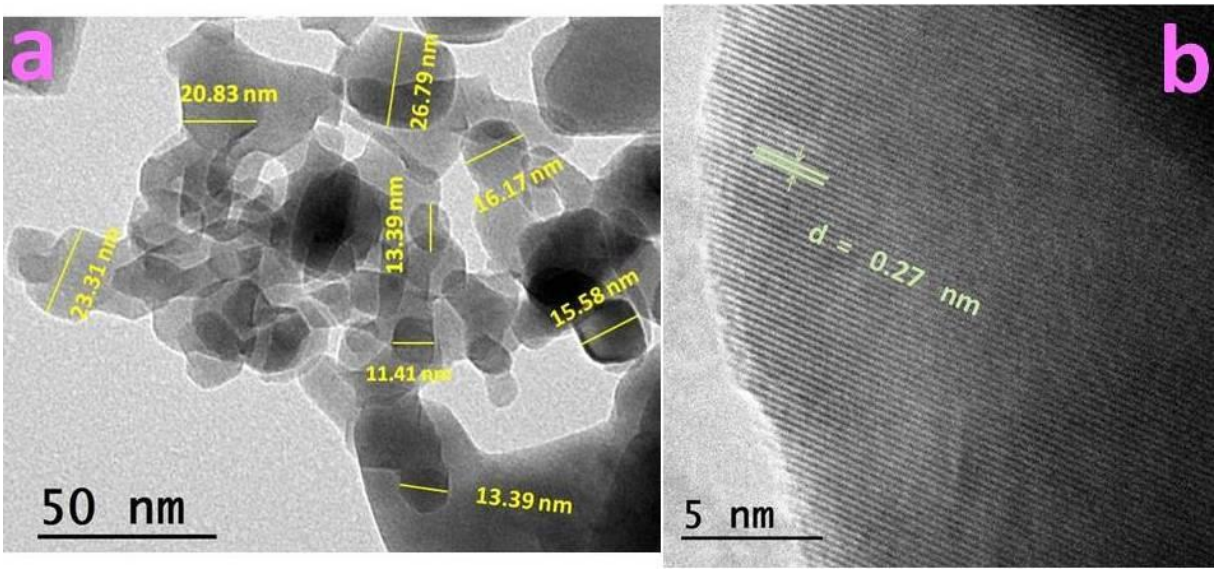


Fig. 2

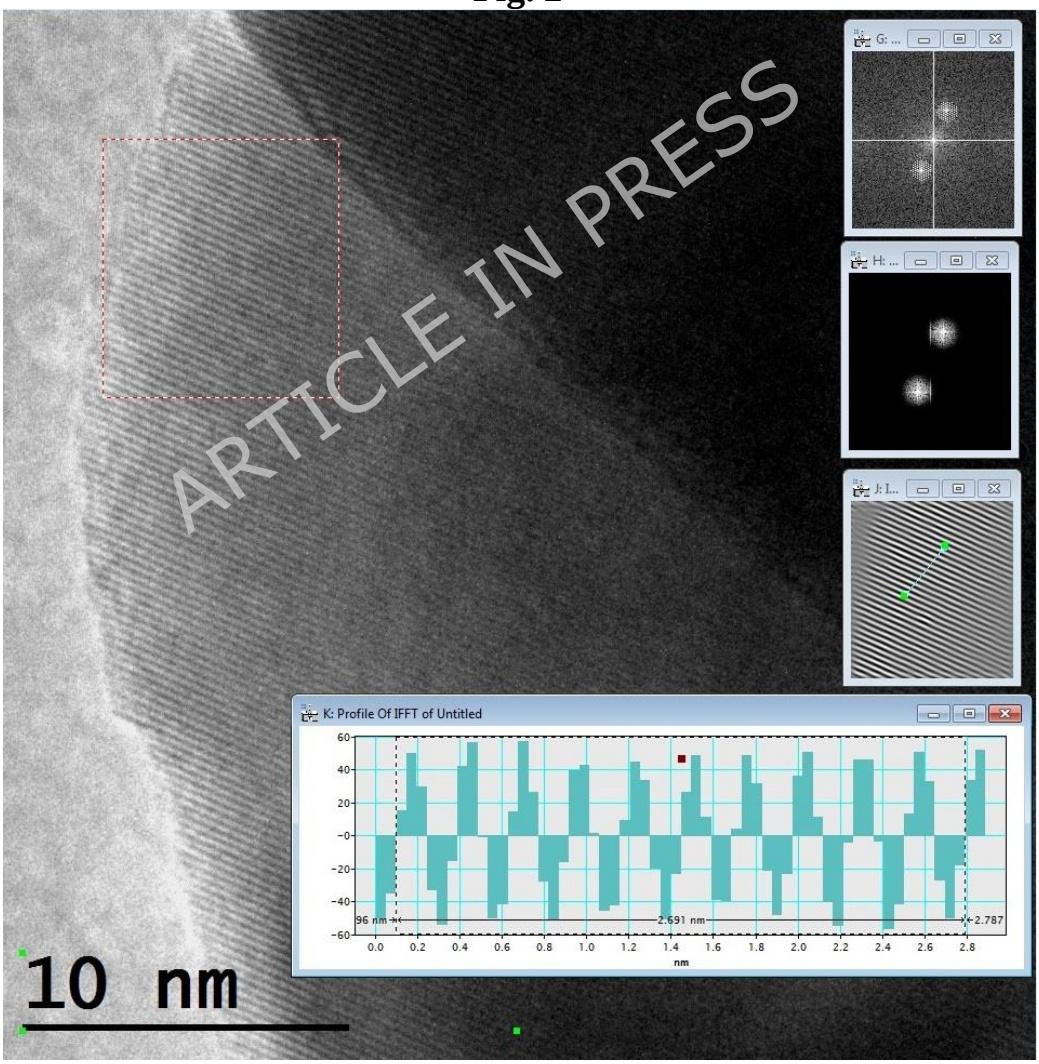


Fig. 3

ARTICLE IN PRESS

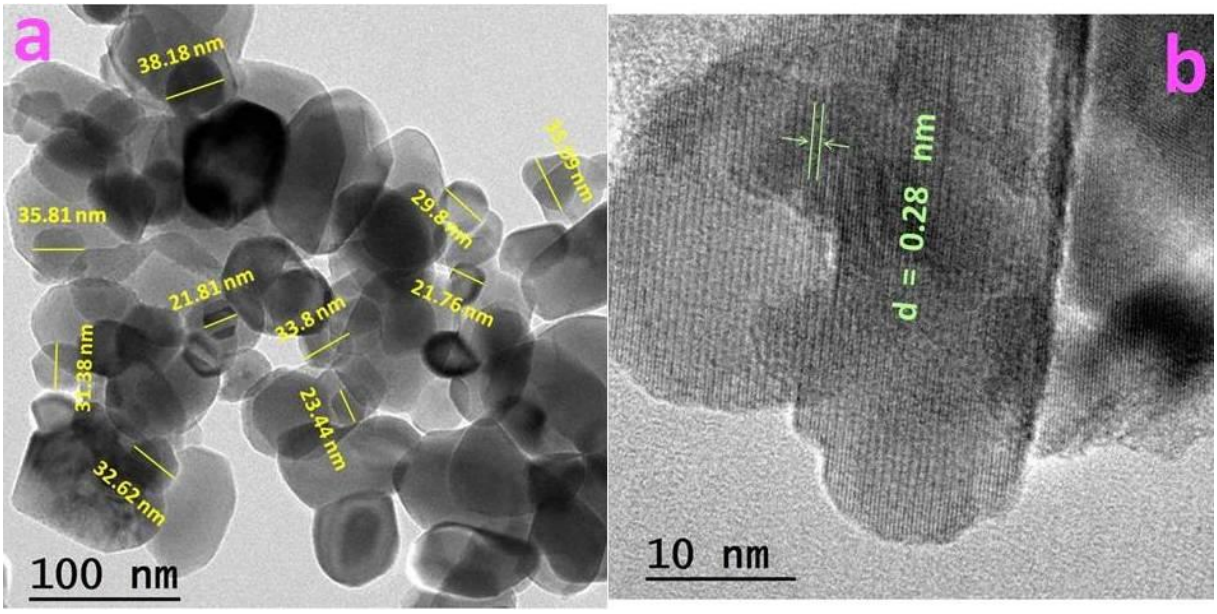

a
38.18 nm
35.81 nm
29.8 nm
21.81 nm
33.8 nm
21.76 nm
31.38 nm
23.44 nm
32.62 nm
100 nm
b
d = 0.28 nm
10 nm

Fig. 4

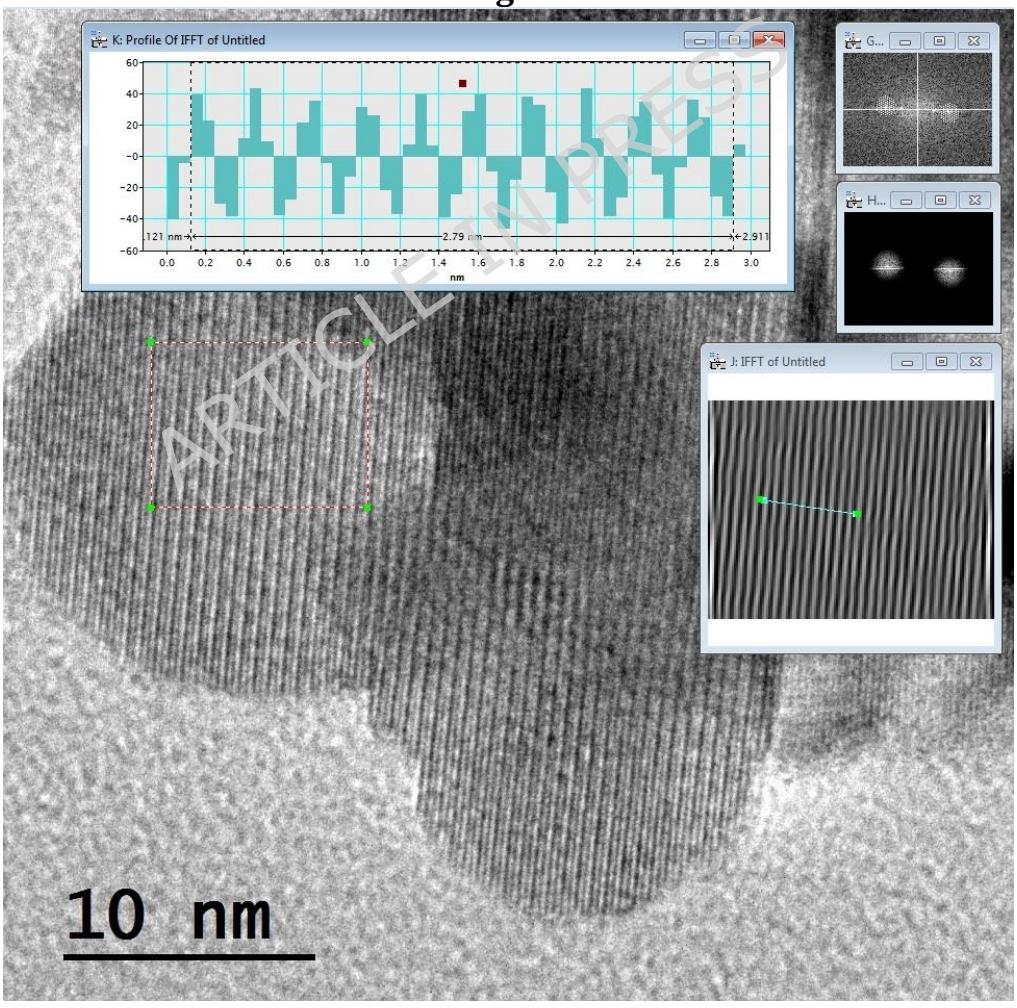

K: Profile Of IFFT of Untitled
G...
H...
J: IFFT of Untitled
10 nm

Fig. 5

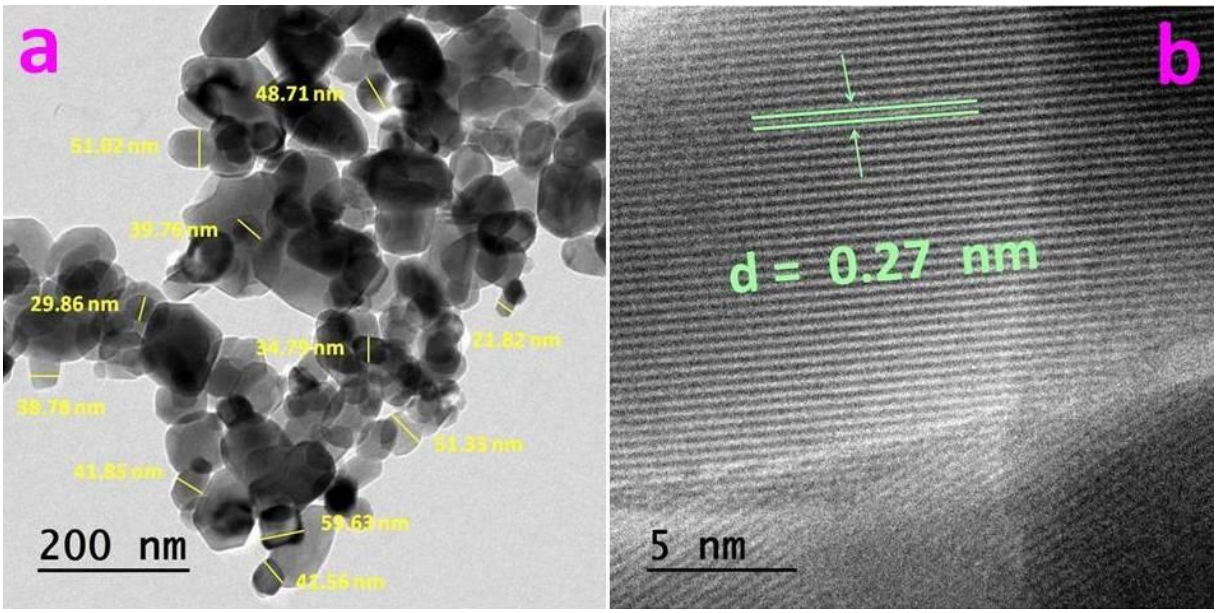

a
48.71 nm
51.02 nm
39.76 nm
29.86 nm
34.79 nm
21.82 nm
38.76 nm
51.35 nm
41.85 nm
59.63 nm
42.56 nm
200 nm
b
d = 0.27 nm
5 nm

Fig. 6

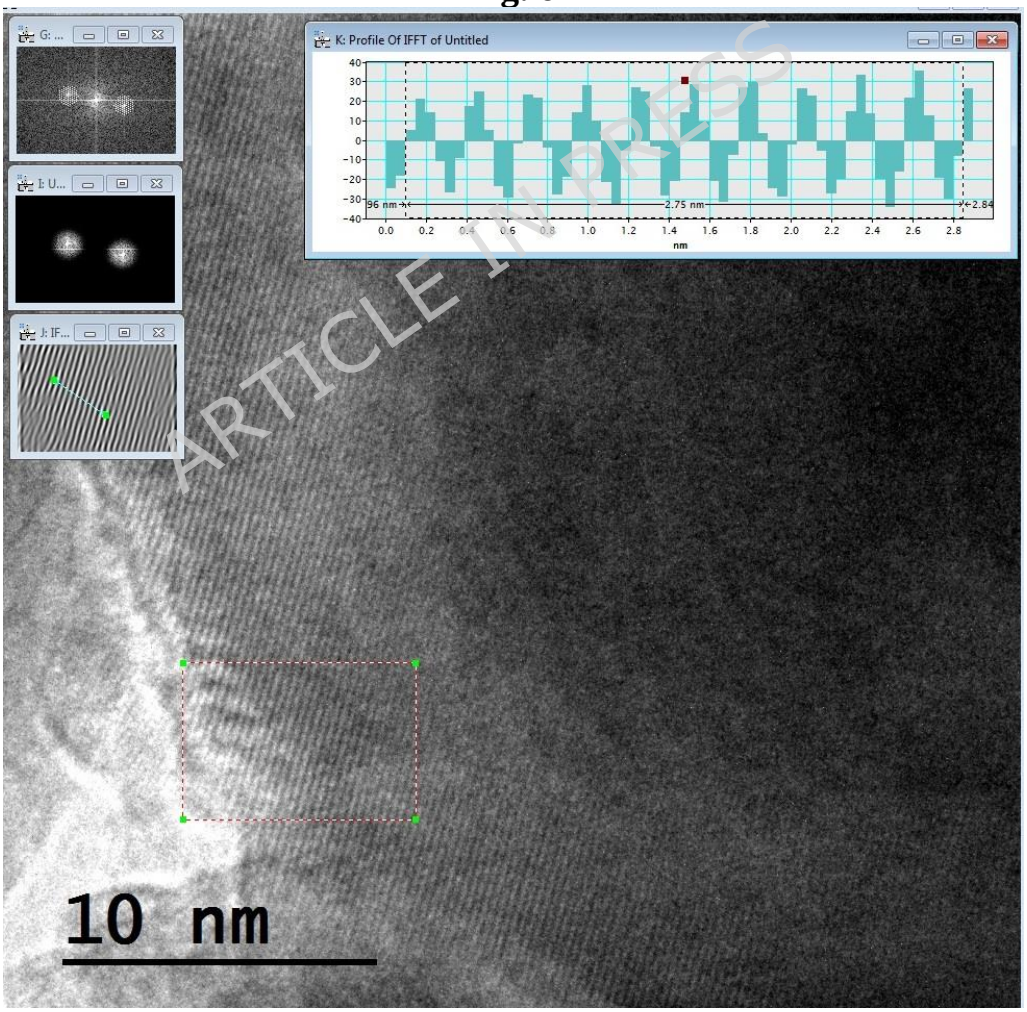

G: ...
I: U...
J: IF...
K: Profile Of IFFT of Untitled
2.75 nm
nm
10 nm

Fig. 7

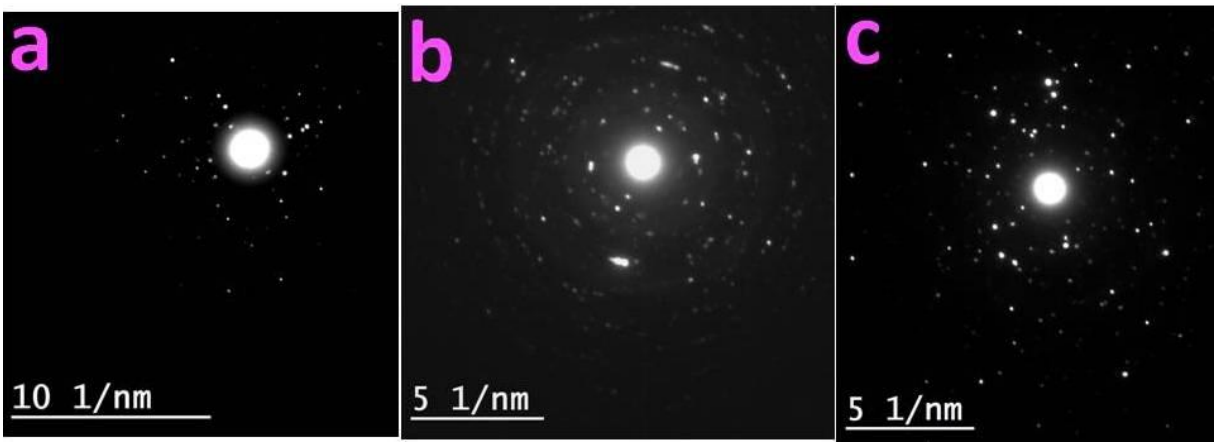

a
10 1/nm
b
5 1/nm
c
5 1/nm

Fig. 8

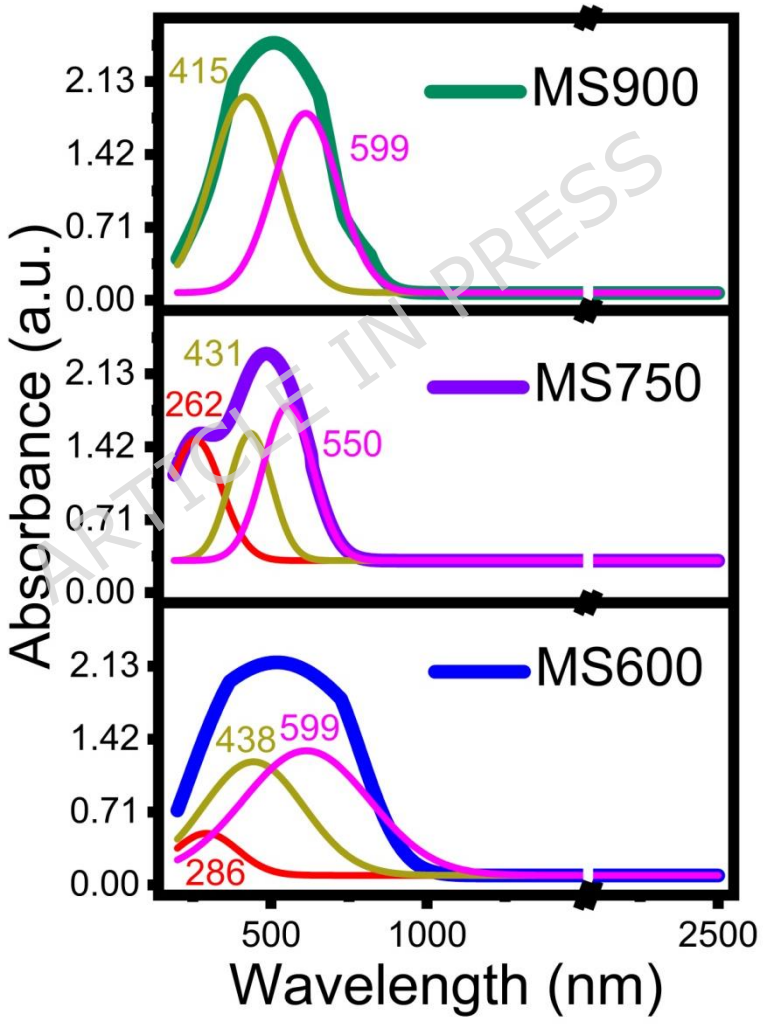

Absorbance (a.u.)
2.13
1.42
0.71
0.00
415
599
MS900
431
262
550
MS750
438
599
286
MS600
500
1000
2500
Wavelength (nm)

Fig. 9

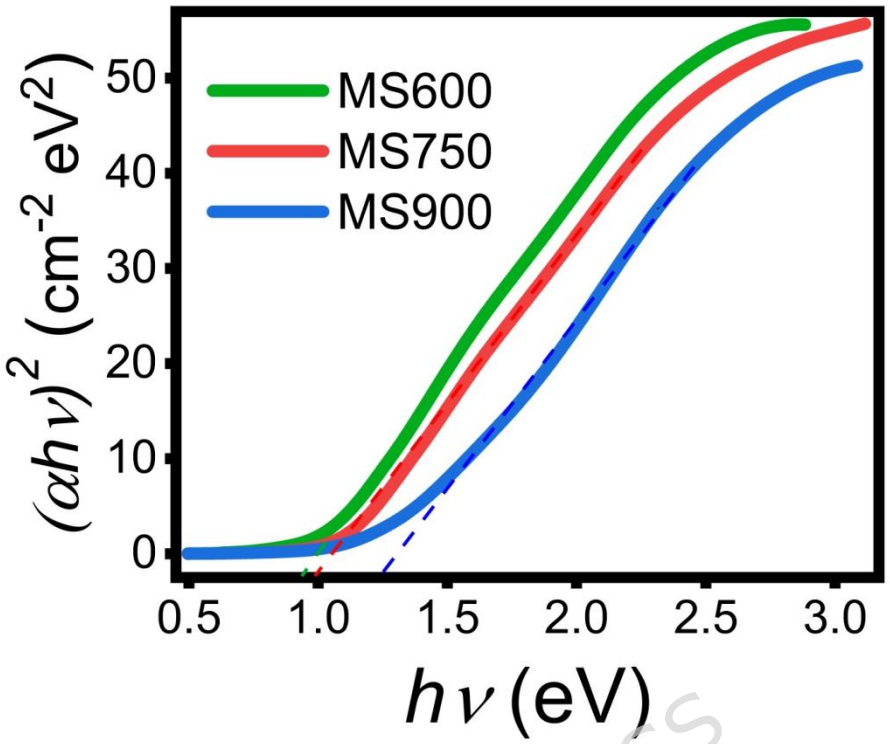

MS600
MS750
MS900
$(\alpha h\nu)^2$ (cm^{-2} eV^2)
$h\nu$ (eV)
0
10
20
30
40
50
0.5
1.0
1.5
2.0
2.5
3.0

Fig. 10

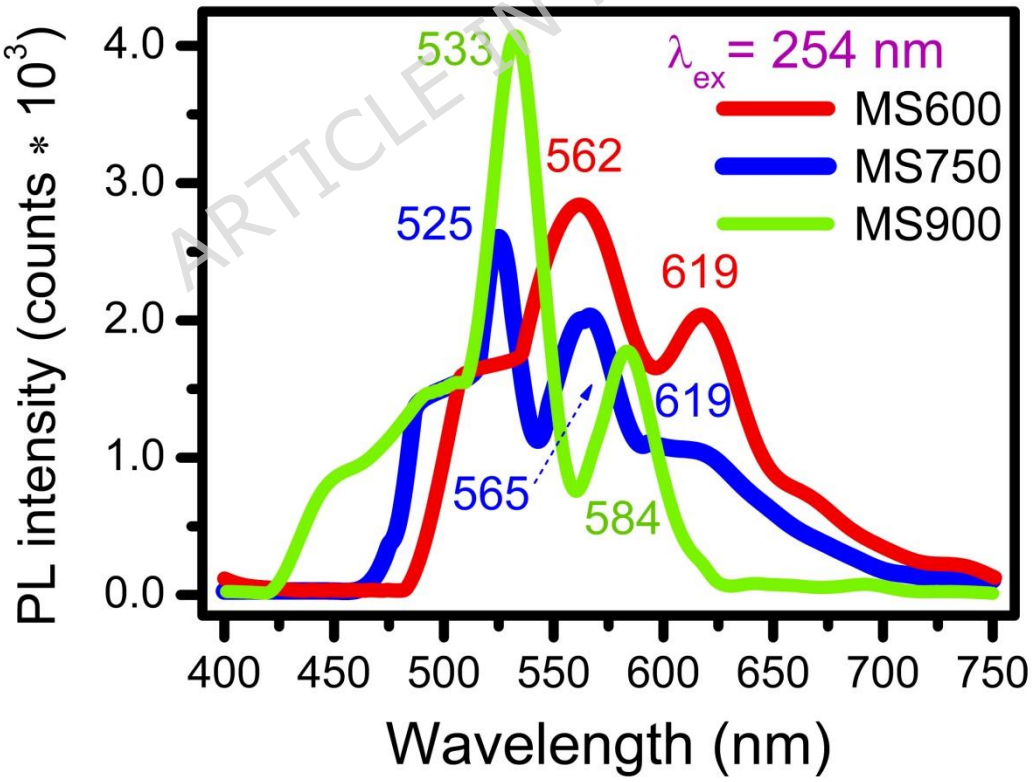

λ_{ex} = 254 nm
MS600
MS750
MS900
533
562
525
619
619
565
584
PL intensity (counts * 10^3)
Wavelength (nm)
0.0
1.0
2.0
3.0
4.0
400
450
500
550
600
650
700
750

Fig. 11

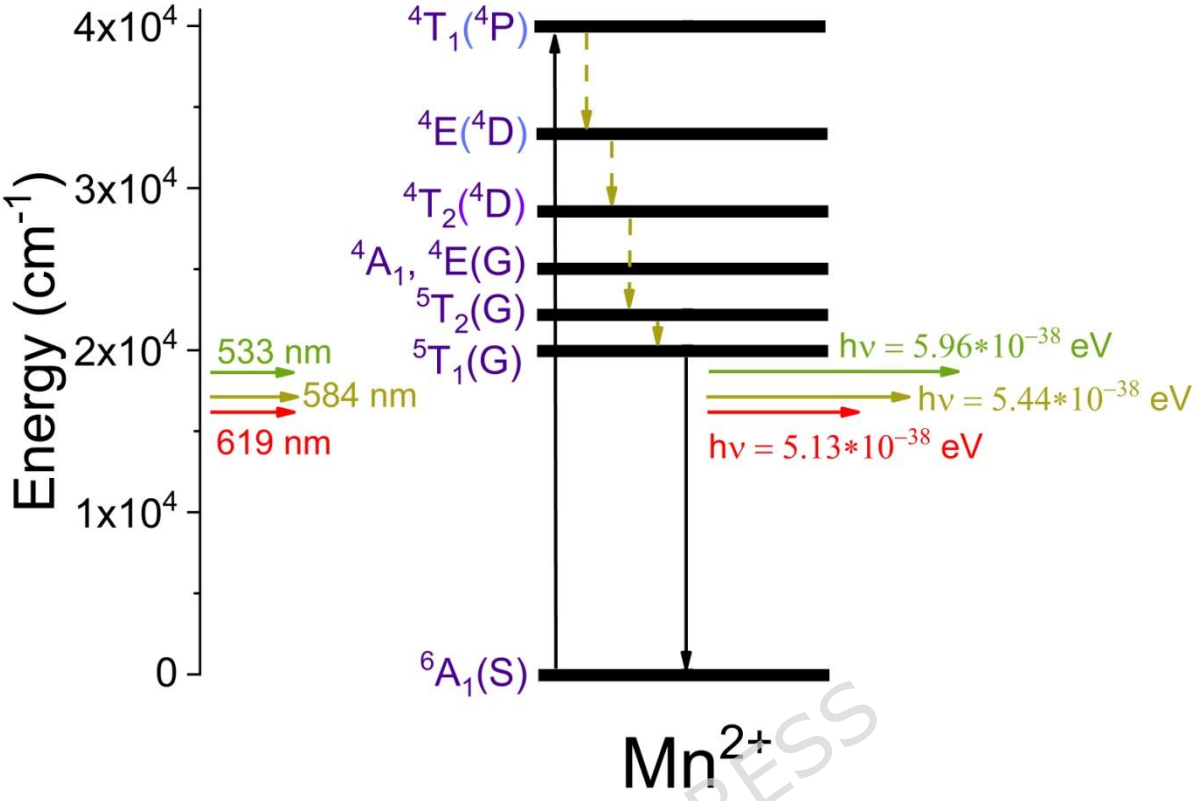

Energy (cm-1)
4x10^4
3x10^4
2x10^4
1x10^4
0
4T1(4P)
4E(4D)
4T2(4D)
4A1, 4E(G)
5T2(G)
5T1(G)
6A1(S)
533 nm
584 nm
619 nm
hν = 5.96*10−38 eV
hν = 5.44*10−38 eV
hν = 5.13*10−38 eV
Mn2+

Fig. 12

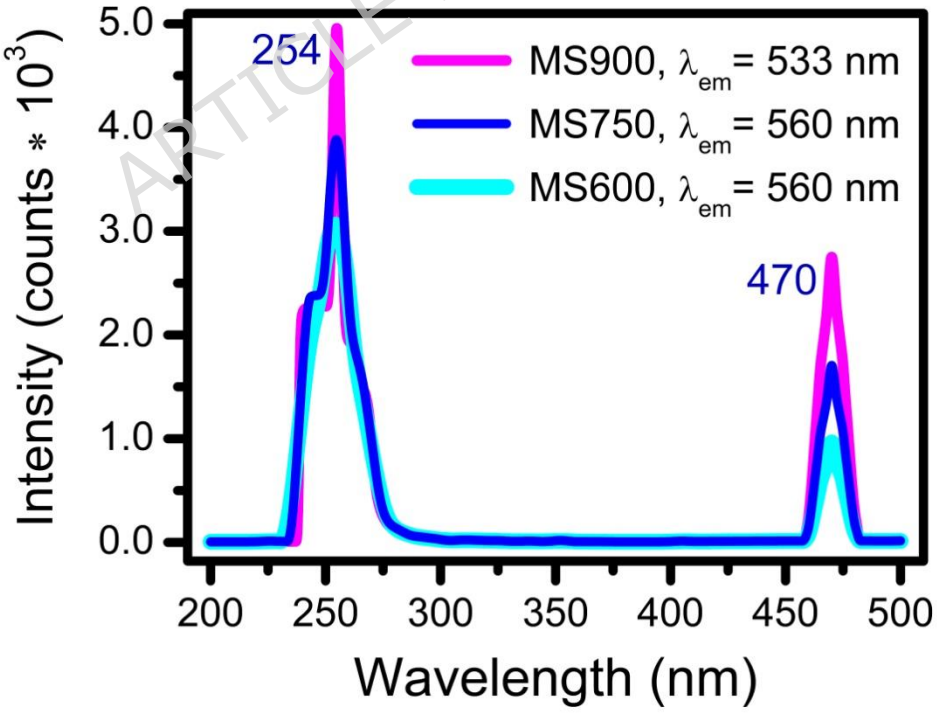

Intensity (counts * 10^3)
5.0
4.0
3.0
2.0
1.0
0.0
254
470
MS900, λem = 533 nm
MS750, λem = 560 nm
MS600, λem = 560 nm
200
250
300
350
400
450
500
Wavelength (nm)

Fig. 13

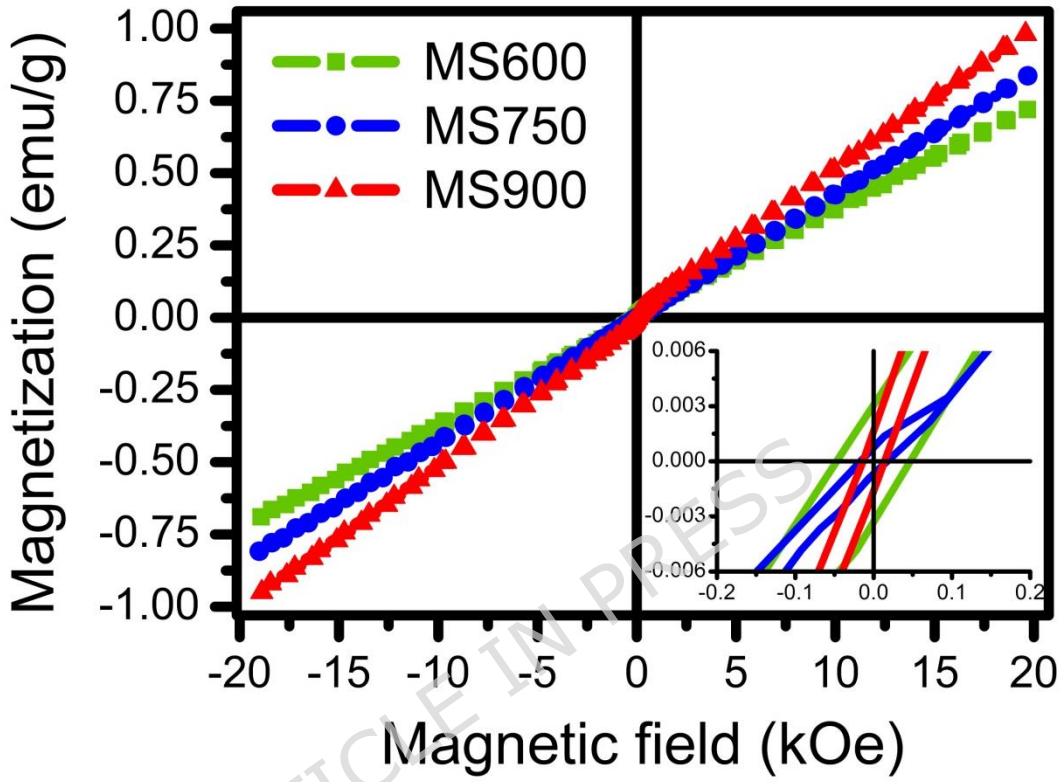


Fig. 14

ARTICLE IN PRESS

Figures captions

Fig. 1. XRD patterns of the Mn_7SiO_{12}–$MnSiO_3$ nanocomposites prepared at 600, 750 and 900 °C.

ARTICLE IN PRESS

Fig. 2. a) TEM image of the MS600 nanocomposite and b) its HRTEM lattice image indicating *d*= 0.27 nm.

Fig. 3. IFFT profile of the MS600 nanocomposite.

Fig. 4. a) TEM image of the MS750 nanocomposite and b) its HRTEM lattice image indicating *d*= 0.28 nm.

Fig. 5. IFFT profile of the MS750 nanocomposite.

Fig. 6. a) TEM image of the MS900 nanocomposite and b) its HRTEM lattice image indicating *d*= 0.27 nm.

ARTICLE IN PRESS

Fig. 7. IFFT profile of the MS900 nanocomposite.

Fig. 8. a,b,c) SAED patterns of the MS600, MS750 and MS900 nanocomposites, respectively.

Fig. 9. Absorbance spectra of the MS600, MS750 and MS900 nanocomposites.

ARTICLE IN PRESS

Fig. 10. Tauc plots for determination of E_g of the MS600, MS750 and MS900 nanocomposites.

Fig. 11. Room temperature PL emission spectra, excited at 254 nm, of the MS600, MS750 and MS900 nanocomposites.

Fig. 12. Schematic diagram of the energy levels of Mn^{2+} illustrating the present fluorescence emission mechanism.

Fig. 13. Excitation spectra of the MS600, MS750 and MS900 nanocomposites monitored at λ_{em}= 560, 560 and 533 nm, respectively.

Fig. 14. Room temperature magnetic M–H hysteresis loops of the MS600, MS750 and MS900 nanocomposites. The inset graph shows their narrow hysteresis loops with non-vanishing coercivity and remanence.

Tables

Table 1

ARTICLE IN PRESS

Chemical composition, sample code, heat-treatment temperature (T) and E_g of the investigated Mn_7SiO_{12}–$MnSiO_3$ nanocomposites

Sample code	Chemical composition (Mol.%)		T (°C)	E_g (eV)
	MnO	SiO_2		± 0.005
MS600	50	50	600 °C	0.935
MS750	50	50	750 °C	0.994
MS900	50	50	900 °C	1.242

Table 2
Crystalline phases constituting the synthesized nanocomposites, their phases fractions and their average crystallite size (D) calculated from XRD analysis

Sample code	Phases	Phases fractions (%)	D (nm) ± 2 nm
MS600	Mn_7SiO_{12}	65.4	22
	$MnSiO_3$	34.6	20
MS750	Mn_7SiO_{12}	60.5	33
	$MnSiO_3$	39.5	29
MS900	Mn_7SiO_{12}	54.8	42
	$MnSiO_3$	45.2	40

ARTICLE IN PRESS

Table 3
Room temperature magnetization parameters of the synthesized MS600, MS750 and MS900

Sample code	Magnetization (emu/g) Ms ± 0.2%	Coercivity (Oe) Hc ± 0.2%	Remanence (emu/g) Mr ± 0.2%
MS600	0.7199	47.01	0.003072
MS750	0.8365	19.04	0.000775
MS900	0.9809	14.61	0.001720

ARTICLE IN PRESS

ARTICLE IN PRESS